ELSEVIER

Catalysis Today 69 (2001) 153–163

CATALYSIS TODAY

www.elsevier.com/locate/cattod

Influence of channel geometry on hydrodynamics and mass transfer in the monolith film flow reactor

A.K. Heibel*, J.J. Heiszwolf, F. Kapteijn, J.A. Moulijn

Delft ChemTech, Industrial Catalysis, Delft University of Technology, Julianalaan 136, 2628 BL Delft, The Netherlands

Abstract

The hydrodynamics and the gas–liquid mass transfer as a function of the channel geometry have been investigated for the monolith film flow reactor. For the hydrodynamic studies, the liquid distribution and the flooding boundaries have been experimentally determined. The liquid distribution improved with increasing liquid flow rate. The flooding limits are in the range of other commercial structured packings and allow operation under industrially relevant conditions. Larger channel sizes and lower surface tension expand the operating window, while viscosity seems to have a minor impact. The gas–liquid mass transfer is a strong function of the surface to volume ratio defined by the channel dimensions. Co- and counter-current flow operation result in similar performance. Furthermore, shorter monoliths, with larger contribution of the inlet section have significant higher mass transfer due to the development of the concentration profile. The obtained $k_{GL}a_V$ values of around $0.01\ s^{-1}$ are in the range of other commercial packings in counter-current flow operation. A three-dimensional single channel model describing the hydrodynamic and diffusion phenomena in the monolith is in good agreement with the experimental results. The flexibility in channel size and dimension allows tailoring the monolith reactor to the specific needs of the individual application.

Keywords: Monolith; Film flow; Flow distribution; Hydraulic capacity; Mass transfer

1. Introduction

The use of structured packings has drawn the attention of researchers from various disciplines in chemical engineering. Monolithic packings, e.g. have found many applications in gas treatment processes such as cleaning of automotive exhaust gases and industrial off-gases. On the other hand, corrugated metal sheet structures have shown to be useful in gas–liquid processes such as absorption and distillation [1]. In the last decade, the use of monolithic structures has been extended to multiphase applications operated in co-current mode and recently also in counter-current mode [1,2].

In monoliths, different flow regimes can occur. Most interesting for industrial applications are bubble or slug flow on the one hand and film flow on the other hand. The separated flow passages of the liquid and the gas in the film flow regime allow besides the co-current also the counter-current operation of the monolith reactor. Targeted applications for this new type of reactor packing are catalytic processes, which have high requirements on catalyst loading and surface to volume ratio. Hereby, the channel geometry and shape of the monolith can be adapted to the needs of the specific application. In this

* Corresponding author. Present address: Corning, Inc., Corning, NY 14831, USA. Tel.: +1-607-974-8430; fax: +1-607-974-4617.
E-mail address: heibelak@corning.com (A.K. Heibel).

0920-5861/01/$ – see front matter
PII: S0920-5861(01)00391-1

Nomenclature

a	surface to volume ratio (m^2/m^3)
A	area (m^2)
c	concentration in the liquid phase (mg/l)
d	diameter (m)
D	diffusion coefficient (m^2/s)
g	gravitational constant (m/s^2)
k	mass transfer coefficient (m/s)
l	length (m)
Δp	pressure drop (Pa)
T	temperature (K)
u	velocity (m/s)
x, y, z	coordinate direction (m)

Greek symbols

γ	uniformity index (–)
η	dynamic viscosity (Pa s)
ρ	density (kg/m^3)
ϕ	volume flow rate (m^3/s)
ω	non-uniformity (–)

Subscripts

c	corner
ch	channel
F	fluid
G	gas
GL	gas–liquid
h	hydraulic
i	local
l	length
L	liquid
mc	mixing cup
Mono	monolith
R	reactor
s	superficial
V	void
x, y, z	coordinate direction
0	reactor based

context, the counter-current operation is especially of interest for processes, where the removal of a gaseous reaction product from the liquid can boost the desired conversion. Examples are processes in which the reaction rate is suppressed by product inhibition (HDS) or limited by thermodynamic equilibrium (HDA). In general, it can be alleged that these structures can be used in processes that combine gas–liquid reaction and separation in one way or another [2].

2. Hydrodynamic and diffusion model description

The monolith can be viewed as an assembly of parallel channels. Under the assumption of a uniform distribution of the gas and liquid phase over the cross-section, a single channel can be considered to describe the hydrodynamic and mass transfer behavior. The Navier–Stokes equation [3] reduces to the Poisson equation for the steady, developed one-directional laminar flow of a Newtonian fluid in the capillary size channel:

$$\eta_F \left(\frac{\partial^2 u_{F,z}}{\partial x^2} + \frac{\partial^2 u_{F,z}}{\partial y^2} \right) = -\frac{dp}{dz} + g\rho_F \quad (1)$$

Accumulation of the liquid in the corners of the square channel with a smooth arc-shaped gas–liquid interface and a contact angle of 0° at the gas–liquid–solid contact line is assumed for the definition of the geometry domain under partially irrigated conditions (Fig. 1A). For full irrigation, a smooth circular gas–liquid interface is assumed (Fig. 1B) [2,4]. The finite element method (FEM) is used to solve Eq. (1) with the no-slip boundary condition at the wall and the gas–liquid interface. The viscosity and density of the fluids are calculated as a function of temperature. The liquid-side

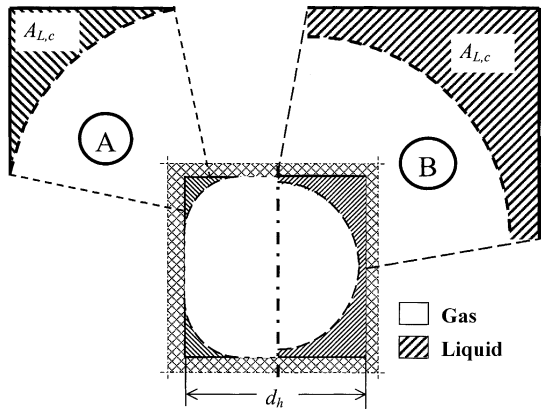

Fig. 1. Gas–liquid domain for hydrodynamic and diffusion modeling: (A) partial irrigation; (B) full irrigation.

contribution of the gas–liquid mass transfer is described by the convection–diffusion equation [3]:

$$u_{L,z}\frac{\partial c_i}{\partial z} = D_i\left(\frac{\partial^2 c_i}{\partial x^2} + \frac{\partial^2 c_i}{\partial y^2}\right) \quad (2)$$

The diffusion component in flow direction is neglected, because of the dominating effect of the convection contribution. Due to the fact that all the mass transfer resistance is assumed to result from the diffusion in the liquid, only the liquid part of the fluid domain is considered. This approach is especially valid for gases with low solubility in the liquid phase (e.g. oxygen in water) or any single component gas phase. Furthermore, gas-saturated liquid is set as a boundary condition at the gas–liquid interface and the Neumann or zero-flux boundary condition is applied at the wall. The developed velocity profile obtained from the solution of Eq. (1) is used as input for the diffusion modeling assuming fully stripped liquid at the inlet. A diffusion coefficient of $2.33 \times 10^{-9}\,m^2/s$ for oxygen in water at room temperature is assumed. The temperature dependency of the binary diffusion coefficient is based on the Stokes–Einstein equation [5]:

$$D_{O_2-H_2O} \propto \frac{T}{\eta_{H_2O}} \quad (3)$$

3. Experimental

3.1. Materials

Different monoliths supplied by Corning, New York were subjects of the investigation. The ceramic monolith material is cordierite ($2MgO{\cdot}2Al_2O_3{\cdot}5SiO_2$) with a porosity around 30%. A summary of the monolith geometry parameters together with a visual indication is presented in Fig. 2.

The monolith structures had a diameter between 42 and 44 mm. The distribution experiments have been performed with a 25 cpsi (cells per square inch) monolith with a length of 250 mm. For the flooding experiments, monoliths with a length of 500 mm were used. Additionally, a length of 80 mm was investigated for the mass transfer measurements to deduct the effects of the liquid distribution and collection section on the mass transfer performance. For all counter-current measurements, the monoliths were equipped with an outlet device to allow effective drainage of the liquid at the bottom of the monolith [2,7]. The flooding behavior was mainly studied with *n*-decane as liquid, however, selective experiments were performed with a 25% glycerol–water mixture and water. The gas–liquid mass transfer experiments were performed with

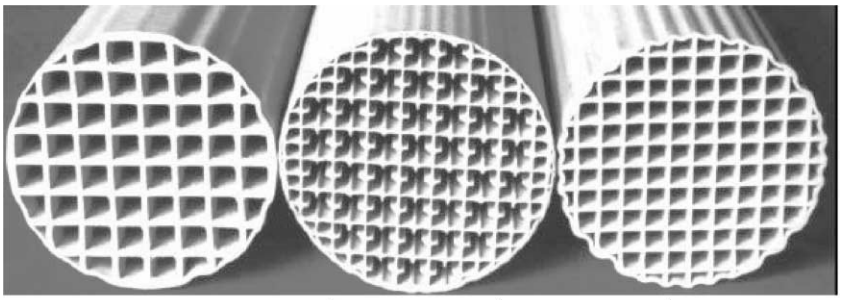

Cell Density [cells/in²]	25	25	50
Shape	Square	Square finned	Square
Void fraction [%]	66	73	68
Surface/volume ratio [m²/m³]	640	1040	920
Hydraulic diameter [mm]	4.14	2.81	2.96
Number of full channels	44	44	88

Fig. 2. Monolith properties.

Table 1
Physical properties [4] of the applied fluids at 20°C and 1.015 bar_a

	Density (kg/m^3)	Dynamic viscosity (Pa s)	Surface tension (mN/m)
n-Decane	730	0.95×10^{-3}	24
Water	998	1.0×10^{-3}	71
25% glycerol–water	1050	2.0×10^{-3}	70
Air	1.2	18.0×10^{-6}	–
Nitrogen	1.15	17.5×10^{-6}	–

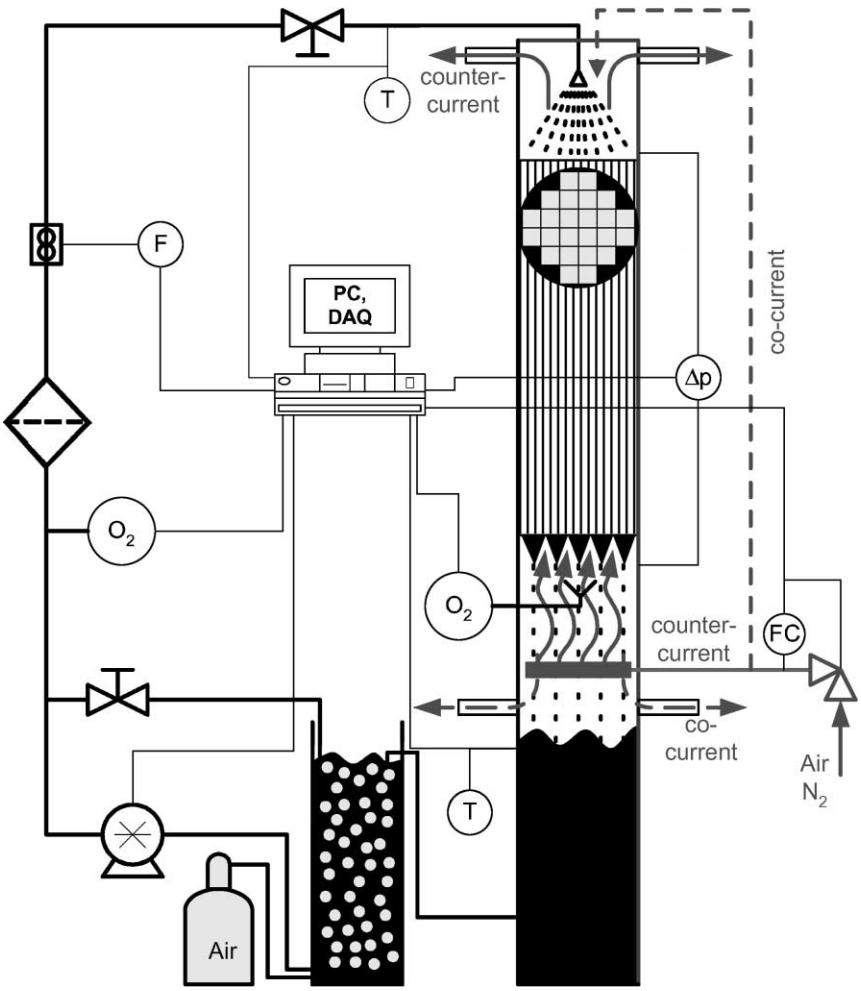

Fig. 3. Experimental set-up.

water as liquid medium. Compressed air was used as the model gas for the flooding experiments and nitrogen for the mass transfer studies. The physical properties of the fluids are summarized in Table 1.

3.2. Experimental set-up and procedures

The liquid was circulated with a gear pump and the flow was measured via a turbine flow sensor. A spray nozzle distributed the liquid over the monolith, which was fixed in a glass tube and sealed at the outside to prevent bypass. The gas was supplied with a mass flow controller and the pressure drop was measured via differential pressure transmitters. The oxygen concentration in the liquid was determined based on fluorescence quenching of a thin film-coated fiber optics probe by oxygen. Data acquisition and control of the set-up was performed with a personal computer (Fig. 3).

For the liquid distribution, the liquid from the individual channels of a 25 cpsi monolith was collected over a certain time period and the volume was determined. This allowed the calculation of the average liquid velocity in each channel during the time period of liquid collection. The same distribution section as for the other experiments has been used, to diminish the effect of any geometrical changes. However, the measurement method did not allow the introduction of any gas flow.

The flooding limits were determined by changes in pressure drop. Therefore, at a given liquid flow rate the gas flow rate was increased in steps. After a stabilization period (15 s), the measurement was performed (15 s). After reaching a pressure drop limit, the gas flow rate was decreased in steps, to determine deflooding.

The gas–liquid mass transfer measurements have been performed in co- and counter-current flow mode. The liquid was saturated with oxygen, by bubbling it with a high flow rate of air in a tank with special sparging devices. The oxygen concentration in the measurement line is continuously monitored to guarantee consistent inlet conditions. Below the outlet of the monolith, a special funnel was installed to allow quick and complete separation of gas and liquid. A frequent two-point calibration of the oxygen sensors (100% saturated and 100% stripped water) was performed to assure the required accuracy.

4. Results and discussion

4.1. Flow distribution

Flow distribution over the cross-section is a critical concern for the application of multiphase monolith reactors. For the film flow operation, especially the distribution of the liquid phase has to be considered. A local non-uniformity is defined to describe the deviation of the local liquid velocity from the average [6]:

$$\omega_{\mathrm{L,i}} = \left| \frac{u_{\mathrm{L,i}} - \bar{u}_{\mathrm{L}}}{\bar{u}_{\mathrm{L}}} \right| \tag{4}$$

The global non-uniformity simply results from integration over the cross-section

$$\omega_{\mathrm{L}} = \frac{\iint_{A_{\mathrm{Mono}}} \omega_{\mathrm{L,i}} \, \mathrm{d}A}{A_{\mathrm{Mono}}} \tag{5}$$

From the non-uniformity, the uniformity index is calculated:

$$\gamma_{\mathrm{L}} = 1 - \tfrac{1}{2}\omega_{\mathrm{L}} \tag{6}$$

The uniformity index ranges from 0 to 1. A value of zero describes a totally mal-distributed flow (i.e. all the liquid flows through one channel), on the other hand a value of 1 results from a perfect distribution.

In Fig. 4, the measured uniformity indices for the different nozzles for *n*-decane are illustrated. It should be mentioned that the uniformity of the liquid distribution is quite sensitive to the distance between nozzle tip and monolith inlet cross-section. For each flow rate, four different heights have been investigated to find the optimum nozzle position. The results in Fig. 4 are based on the optimum nozzle position, dependent on the distributor and the liquid flow rate. In general, the measurements were repeatable with a tolerance of ± 0.01 in uniformity index.

High values of the uniformity index between 0.85 and 0.95 are obtained for the macroscopic distribution over the monolith cross-section. Independent of the distributor, higher flow rates result in better liquid distribution. Detailed analysis of the distribution patterns showed that for the optimum nozzle height, the areas of low and high local velocities are rather randomly spread over the monolith cross-section. Only the distributor for low liquid flow rates showed a distinct pattern of low flow in the center of the monolith.

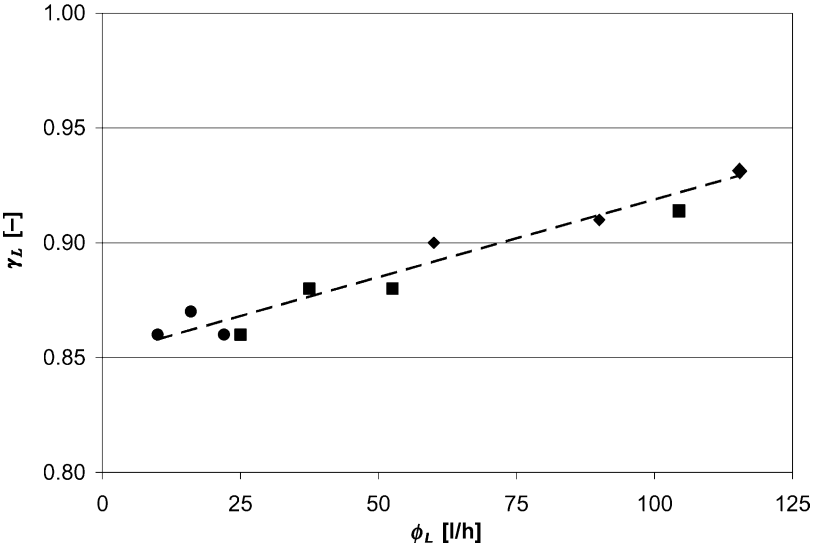

Fig. 4. Uniformity index as a function of the liquid flow rate and different distributors (●, ■, ◆) for *n*-decane, 20°C, 1 bar_a.

4.2. Flooding limits

In general, flooding describes the transport of the liquid phase against its desired flow direction due to the counter-current flow of the gas phase. There is no strict definition of flooding. Different approaches have been taken to determine flooding, based on hydrodynamic, mass transfer or separation performance and stability of operation [8].

In the context of this work, hydrodynamic flooding was considered. The pressure drop as a function of gas flow rate for a low and a high liquid flow rate are summarized in Fig. 5. At flooded conditions slugging of the liquid phase occurs in the individual

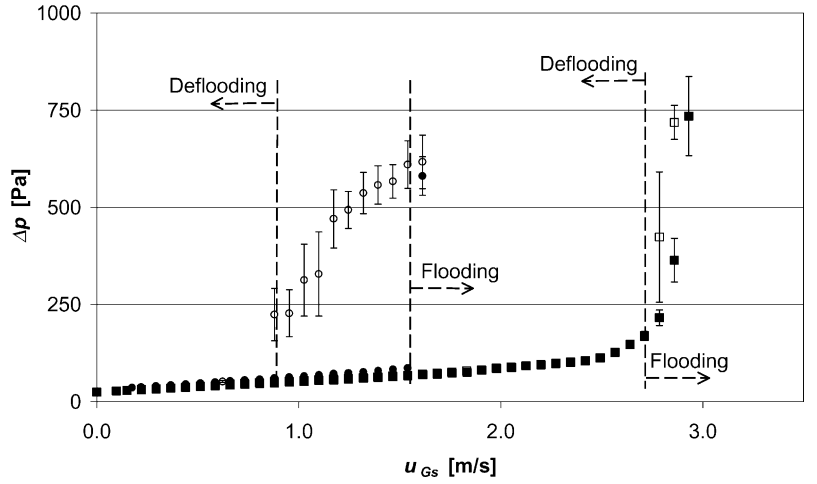

Fig. 5. Pressure drop and fluctuations as a function of superficial gas velocity for low and high liquid velocity with indication of flooding and deflooding point: (■) $u_{Ls} = 0.65$ cm/s increasing gas flow; (□) $u_{Ls} = 0.65$ cm/s decreasing gas flow; (●) $u_{Ls} = 4.75$ cm/s increasing gas flow; (○) $u_{Ls} = 4.75$ cm/s decreasing gas flow; *n*-decane/air, 25 cpsi, 500 mm length, 20°C, 1 bar_a.

channel, which results in a large pressure drop and the occurrence of pressure drop fluctuations. These criteria were applied to evaluate the operating boundaries of the monolith film flow reactor. A linear increase in pressure drop with gas flow rate was determined in the non-flooded region, as expected for laminar flow. Small fluctuations in pressure drop were observed, indicating the steadiness of this flow pattern. Approaching the onset of flooding, a somewhat different behavior for the two liquid flow rates is experienced. First of all for the lower liquid flow rate flooding starts at significant higher gas flow rates. Additionally, there is a rather smooth transition to the flooding point, with a more gradual increase in pressure drop. Lebens et al. [2,9] attributed this behavior to the onset of flooding in the bottom section of the monolith, which breaks down over the length of the monolith and does not propagate to the top.

Summarizing the flooding points for increasing gas velocity from the individual experiments, a flow map indicating the operating window can be established (Fig. 6). The limiting gas velocity for non-flooded operation increases exponentially for lower liquid velocities. Major differences are experienced between the aqueous media and the organic liquids. Further comparison between the two aqueous solutions implies only moderate sensitivity of the flooding behavior on the dynamic viscosity.

Fig. 7 shows the hydraulic capacity plot for different channel sizes and shapes comparing different data sets from literature and the current experimental study. According to their similarity in hydraulic diameter, the flooding limits of the 50 cpsi and internally finned monolith (IFM) are in the same range. A slight deviation in the shape of the flooding curve might be most likely attributed to the differences in channel shape and the applied outlet device. A much broader operating window was obtained for the 25 cpsi monolith, resulting from the larger hydraulic diameter. A similar shape of the flooding curves is observed for the two square cell geometries. Under the assumption that the flooding performance of the KATAPAK-S structure is similar for the fluid system *n*-decane/air compared to water/air, the hydraulic capacity of the 50 cpsi monolith is in-line with the performance of the KATAPAK-S structure ($d_{h,\,ch} = 7$ mm) as reported by Ellenberger and Krishna [10]. Furthermore, all the investigated monolith packings fulfill the operating window requirements for reactive stripping. With the application of the larger hydraulic diameter of the 25 cpsi monolith, the needs for catalytic distillation [11] are achieved.

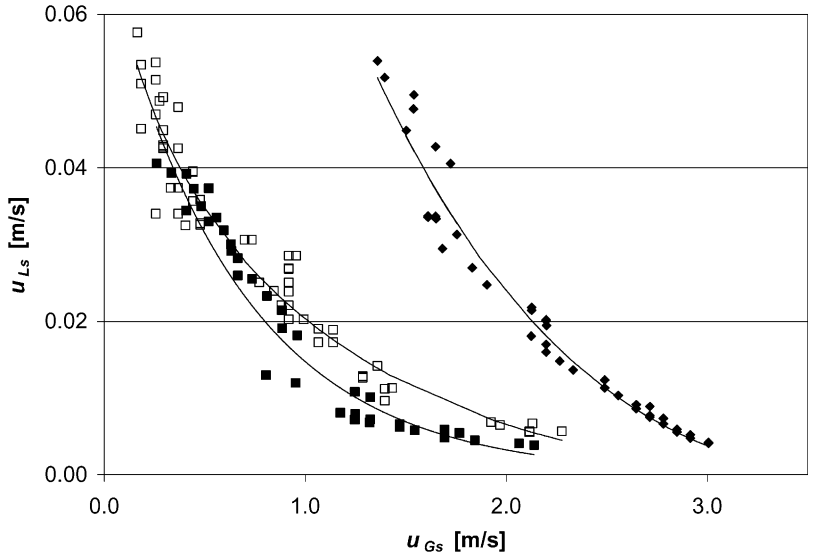

Fig. 6. Flooding transitions for increasing gas flow rates as a function of superficial gas and liquid velocity for different fluids: (◆) *n*-decane/air; (□) water/air; (■) 25% glycerol in water/air; lines represent best fit, 25 cpsi, 500 mm length, 20°C, 1 bar_a.

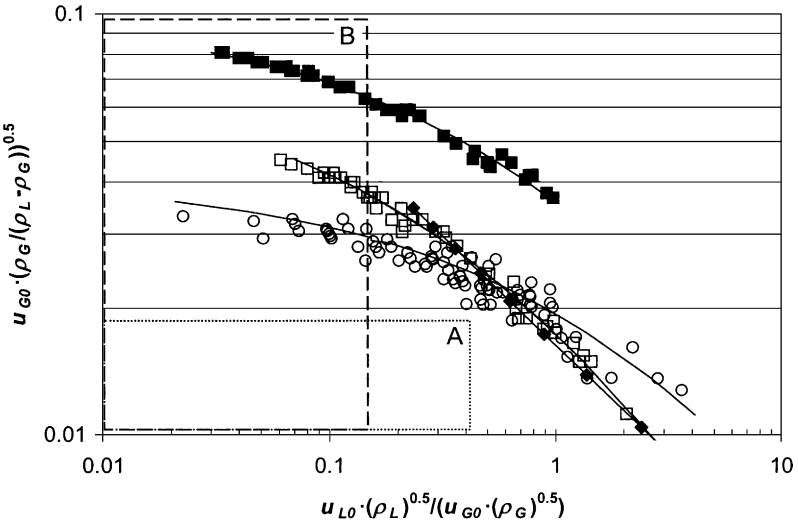

Fig. 7. Hydraulic capacity plot for different cell density and shape monoliths and KATAPAK-S structured packing (■) 25 cpsi, *n*-decane/air; (□) 50 cpsi, *n*-decane/air; (○) IFM, *n*-decane/air [7]; (◆) KATAPAK-S, water/air [10]; lines represent best fit; (A) working area for reactive stripping [2]; (B) working area reactive distillation [11].

4.3. Gas–liquid mass transfer

The gas–liquid mass transfer is an important performance parameter for the application of monolith reactors in three-phase applications. A plug flow reactor model is assumed to calculate the average $k_{GL}a$-value from the experimental and modeling data. Two different representations have been chosen, one based on the void fraction of the packing and the other one based on the overall reactor volume:

$$k_{GL}a_V|_l = \frac{u_{Ls}}{l}\ln\left(\frac{c_{in}}{c_{out}}\right),$$
$$k_{GL}a_R|_l = \frac{u_{L0}}{l}\ln\left(\frac{c_{in}}{c_{out}}\right) \quad (7)$$

To separate liquid distribution and collection effects, a short monolith piece was measured and deduced for the determination of the $k_{GL}a$-value of the considered monolith section:

$$k_{GL}a|_{l_1-l_2} = \frac{k_{GL}a|_{l_2}\cdot l_2 - k_{GL}a|_{l_1}\cdot l_1}{l_2 - l_1} \quad (8)$$

For the model calculations, an average concentration has to be determined at a given axial location. The differences in local velocity have to be taken into account, therefore the mixing-cup concentration is defined [12]:

$$c_{mc} = \frac{\iint_{dA} u_L(x,y)c(x,y)\,dx\,dy}{\phi_L} \quad (9)$$

The effect of the counter-current gas flow was investigated by keeping the liquid flow rate constant and increasing the gas flow (Fig. 8). Due to the separated flow passages of gas and liquid and therefore the low interaction of the two fluids, the outlet oxygen concentration is basically independent of the gas flow rate in the film flow regime, which was also confirmed by modeling calculations. This is also in good agreement with the conclusions of Lebens et al. [13]. At the flooding point, which is indicated by the increase in pressure drop a decrease in the outlet oxygen concentration was determined, due to the change in flow regime. In Fig. 9, the mass transfer performance is illustrated for co- and counter-current flow. Basically, identical performance was obtained for both flow operations. The modeling results are in good agreement with the experimental data. A slight increase in mass transfer is experienced with an increase in liquid flow rate. This behavior is mostly due to the expansion of the liquid pocket in the corner and therefore an

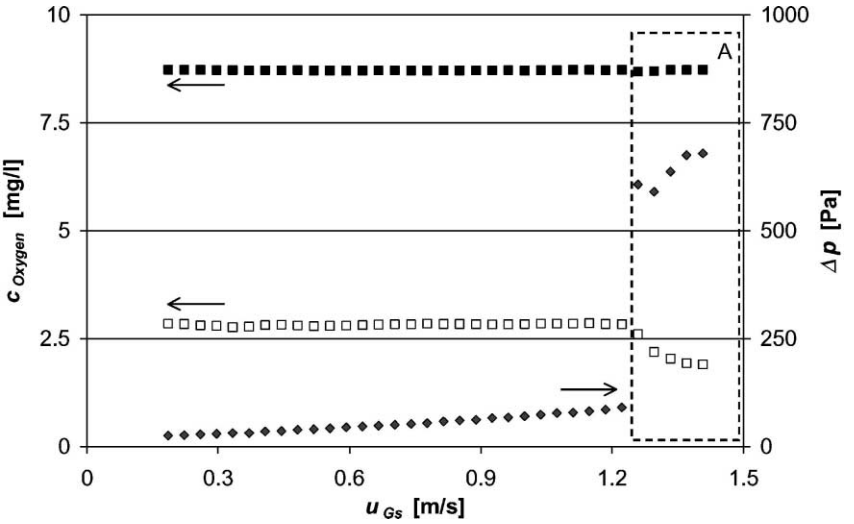

Fig. 8. Oxygen concentration and pressure drop as a function of the superficial gas velocity in stripping experiment (including distribution and collection section): (■) oxygen concentration at the inlet; (□) oxygen concentration at the outlet; (◆) pressure drop; (A) operation under flooding conditions; 25 cpsi, 500 mm length, $u_{Ls} = 1.9$ cm/s, water/air, 20°C, 1 bar_a.

increase in the gas–liquid interfacial area. From this preliminary study, it was concluded that it is also feasible to perform the experiments in co-current film flow mode, which proved to be more reproducible.

Fig. 10 summarizes the experimental data for the 25 and 50 cpsi square cell monoliths. Again good agreement between experimental and modeling results is achieved. The mass transfer is a strong function of

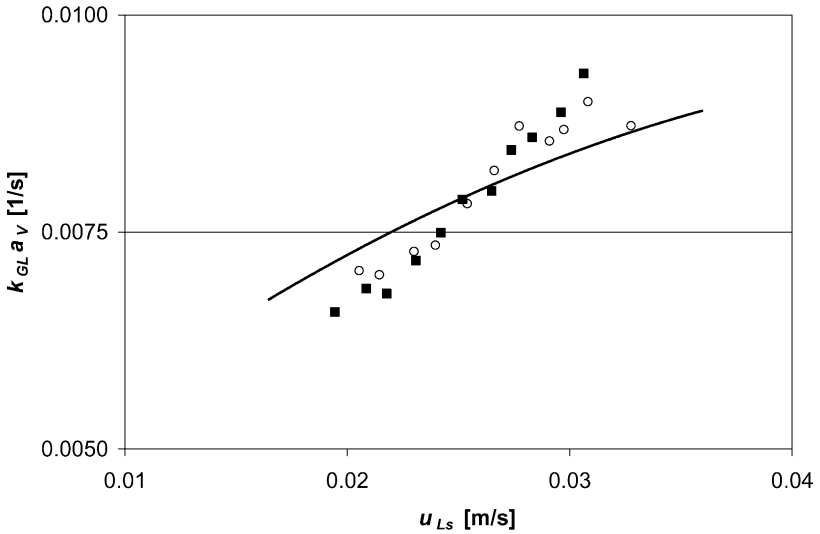

Fig. 9. Gas–liquid mass transfer performance for co- and counter-current gas flow operation: (■) co-current; (○) counter-current; line represents model calculation, $u_{Gs} = 0.75$ m/s, 25 cpsi, 80–500 mm length section, water/air, 12.5°C, 1 bar_a.

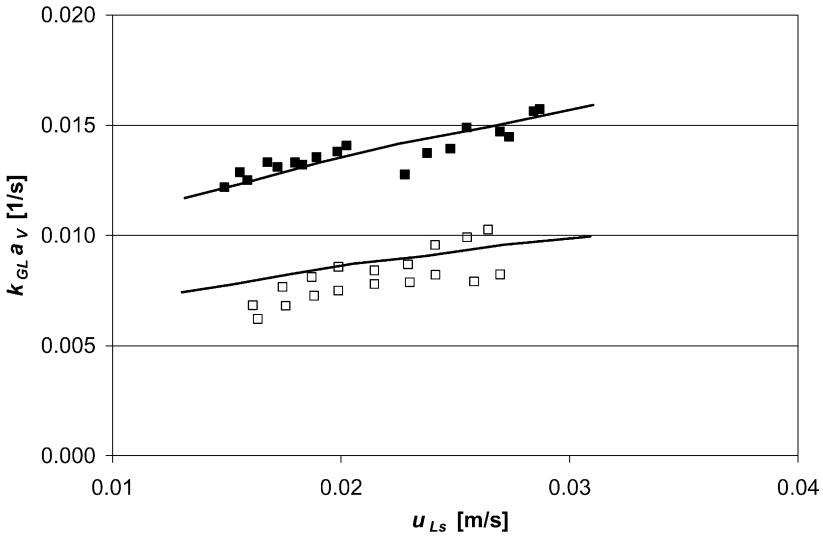

Fig. 10. Experimental and modeling results of the gas–liquid mass transfer performance of 25 and 50 cpsi square monoliths: (■) 50 cpsi monolith; (□) 25 cpsi monolith; lines represent model calculations, $u_{Gs} = 0.75\,m/s$, 80–500 mm length section, water/air, 20°C, 1 bar_a.

the channel dimensions. The higher surface to volume ratio of the 50 cpsi monolith compared to the 25 cpsi one results in an increased gas–liquid interfacial area and a longer average residence time. Therefore, $k_{GL}a_V$-values between 0.012 and 0.015 s^{-1} are found for the 50 cpsi monolith compared to 0.0075–0.01 s^{-1} for 25 cpsi, respectively.

For an accurate determination of the experimental mass transfer values, it was necessary to deduce the liquid distribution and collection effects by measuring a short monolith section. However, due to the development of the concentration profile, a very high mass transfer is apparent in the inlet section. Therefore, a modeling study, including the inlet section, has been

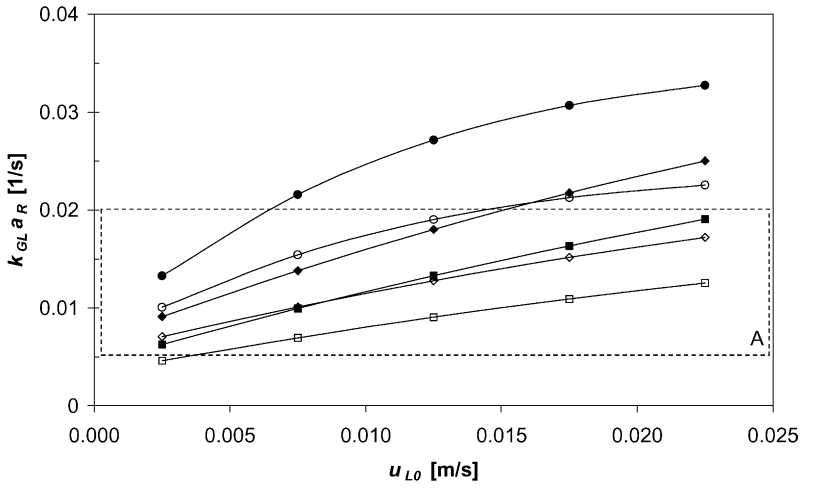

Fig. 11. Modeled mass transfer for different cell shapes and dimensions as a function of monolith length and liquid load: (■) 25 cpsi, 0–250 mm; (□) 25 cpsi, 0–500 mm; (◆) 50 cpsi, 0–250 mm; (◇) 50 cpsi, 0–500 mm; (●) IFM 0–250 mm; (○) IFM 0–500 mm, lines represent best fit; (A) typical $k_{GL}a_R$-values of counter-current packings from Lee and Tsui [14], water/air, 20°C, 1 bar_a.

performed to compare the overall mass transfer performance of the different geometries studied in this paper (Fig. 11). The mass transfer for the IFM was determined from the Sherwood correlation of Lebens et al. [13], which includes the effect of monolith length. The entrance effect is quite evident by comparing the two different lengths for the same geometry option. Clearly, the shorter monolith provides a much higher mass transfer, due to the larger contribution of the entrance region. The performance differences of the three structures scale roughly with the surface to volume ratio. Furthermore, a slight difference in the shape of the $k_{GL}a_R$ curve of the IFM is apparent at higher liquid loads, due to an earlier change from partial to full irrigation [2,13]. The $k_{GL}a_R$ values of all the monolith structures are in the typical range of counter-current packings [14]. Especially, the higher cell density and the IFM operate at the higher range.

5. Conclusions

From the aspects mentioned before, it can be concluded that the monolith film flow reactor is a valid option for three-phase catalytic reactions. In general, the flexibility in cell shape and dimension allow the application of the monolith film flow reactor over a wide range of conditions and process requirements. A high surface to volume ratio can be achieved, which will be especially beneficial for catalytic applications, where short diffusion lengths are very important.

With appropriate distribution devices and positioning of them, a uniform distribution over the cross-section of a monolith is obtained. This is an essential condition for performing unbiased experiments. In general, a better distribution is obtained with higher flow rates. This implies that the distribution issue is especially a concern for small-scale testing, and might be overcome for larger-scale applications.

The hydraulic capacity of the monolith reactor is very dependent on the liquid drainage. With an appropriate outlet device an operating window, interesting for industrial application, is achieved. The hydraulic capacity scales with the hydraulic diameter of the monolith channel. A strong effect of the surface tension of the liquid is apparent, however, the effect of viscosity is rather small. Furthermore, comparable flooding performance to other advanced structured packings is obtained.

Mass transfer measurements resulted in k_La_V-values in the range 0.0075–0.015 s^{-1}, which are in the range of other packings operated in counter-current flow [14]. The performance for co- and counter-current film flow operation is similar. The applied two-phase model is in good agreement with the experimental data and seems to capture the trends in flow conditions and properties as well as geometry parameters properly. The low momentum exchange in the film flow regime shows no impact of the gas flow rate and only a slight increase of $k_{GL}a_V$-values with the liquid flow. A strong impact of the geometry parameters is observed. The mass transfer performance scales with the surface to volume ratio. Therefore, modeling calculations predict the highest $k_{GL}a_R$-values for the internally finned structure. Furthermore, shorter monoliths result in higher mass transfer, due to a relatively larger contribution of the development of the concentration profile at the inlet section compared to longer monoliths.

References

[1] A. Cybulski, J.A. Moulijn, Structured Catalyst and Reactors, Marcel Dekker, New York, 1998.
[2] P.J.M. Lebens, Ph.D. Thesis, University of Delft, Delft, the Netherlands, 1999.
[3] L.P.B.M. Janssen, M.M.C.G. Warmoeskerken, Transport Phenomena Data Companion, Delftse Universitaire Pers, Delft, 1997.
[4] W.B. Kolb, Ph.D. Thesis, The University of Tulsa, USA, 1993.
[5] S. Middleman, An Introduction to Mass and Heat Transfer, Wiley, New York, 1997.
[6] A.K. Heibel, M.A.A. Spaid, SAE Paper 1999-01-0768, 1999.
[7] P.J.M. Lebens, M.M. Stork, F. Kapteijn, S.T. Sie, J.A. Moulijn, Chem. Eng. Sci. 54 (1999) 2381–2389.
[8] J.R. Fair, J.L. Bravo, Chem. Eng. Prog. 86 (1990) 19–29.
[9] P.J.M. Lebens, R.K. Edvinsson, S.T. Sie, J.A. Moulijn, Ind. Eng. Chem. Res. 37 (1998) 3722–3730.
[10] J. Ellenberger, R. Krishna, Chem. Eng. Sci. 54 (1999) 1339–1345.
[11] J.L. DeGarmo, V.N. Parulekar, V. Pinjala, Chem. Eng. Prog. 43 (1992) 43–50.
[12] M. Zogg, Verfahrenstechnik 5 (1971) 328–333.
[13] P.J.M. Lebens, J.J. Heiszwolf, F. Kapteijn, S.T. Sie, J.A. Moulijn, Chem. Eng. Sci. 54 (1999) 5119–5125.
[14] S.H. Lee, Y.P. Tsui, Chem. Eng. Prog. 95 (1999) 23–50.